Decorrelation in Interferometric Radar Echoes

Howard A. Zebker, *Senior Member, IEEE*, and John Villasenor, *Member, IEEE*

***Abstract*—A radar interferometric technique for topographic mapping of surfaces promises a high resolution, globally consistent approach to generation of digital elevation models. One implementation approach, that of utilizing a single synthetic aperture radar (SAR) system in a nearly repeating orbit, is attractive not only for cost and complexity reasons but also in that it permits inference of changes in the surface over the orbit repeat cycle from the correlation properties of the radar echoes. Here we characterize the various sources contributing to the echo correlation statistics, and isolate the term which most closely describes surficial change. We then examine the application of this approach to topographic mapping of vegetated surfaces which may be expected to possess varying backscatter over time. We find that there is decorrelation increasing with time but that digital terrain model generation remains feasible. We present such a map of a forested area in Oregon which also includes some nearly unvegetated lava flows, and find that temporal decorrelation contributions to the height errors may be limited to 1.5 and 2.6 m for the forested and lava areas, respectively, if suitable attention is given to experiment design. Such a technique could provide a global digital terrain map.**

I. Introduction

Interferometric radar has been been proposed and successfully demonstrated as a topographic mapping technique by Graham [1], Zebker and Goldstein [2], and Gabriel and Goldstein [3]. A radar interferometer is formed by relating the signals from two spatially separated antennas; the separation of the two antennas is called the baseline. The spatial extent of the baseline is one of the major performance drivers in an interferometric radar system— if the baseline is too short the sensitivity to signal phase differences will be undetectable, while if the baseline is too long additional noise due to spatial decorrelation corrupts the signal. The theory of spatial baseline noise has previously been described by Li and Goldstein [4], and by Rodriguez and Martin [5], and Li and Goldstein have also shown some experimentally measured determinations of the spatial decorrelation noise level. In this paper we will review that work, develop Fourier transform relations between radar impulse response and the baseline and rotation-induced decorrelation functions, and utilize the results in separating the effects of temporally and spatially induced decorrelation. We then will produce a topographic map of a heavily forested area in Oregon, and assess its accuracy considering both spatial and temporal decorrelation. Finally, we will speculate on the utility of the correlation measurement itself as a remote sensing observable.

Manuscript received August 12, 1991; revised February 20, 1992. The research described in this paper was carried out by the Jet Propulsion Laboratory, California Institute of Technology, under a contract with the National Aeronautics and Space Administration.

The authors are with the Jet Propulsion Laboratory, California Institute of Technology, 4800 Oak Grove Drive Pasadena, CA 91109.

IEEE Log Number 9200760.

Two distinct implementation approaches have been discussed for topographic radar interferometers; they differ in how the interferometric baseline is formed. In the first case the baseline is formed by two physical antennas which illuminate a given area on the ground simultaneously— this is the usual approach for aircraft implementations where the physical mounting structures may be spaced for sufficient baseline. This is the approach used by Zebker and Goldstein [2] for the NASA CV-990 radar, and it is also currently used in the TOPSAR topographic mapping radar mounted on the NASA DC-8 aircraft [6]. This implementation has been suggested for spaceborne use by Rodriguez and Martin [5] and informally by others. In this case either the wavelength is chosen to be quite short (< 1 cm), or for longer wavelengths tethered satellites are required to generate a baseline of adequate length [7].

The second type of implementation, which we analyze here, is to utilize a single satellite antenna in a nearly-exact repeating orbit, forming the interferometer baseline by relating radar signals on repeat passes over the same site. Even though the antennas do not illuminate the same area at the same time, if the ground is completely undisturbed between viewings the signals will be highly correlated and a spatial baseline may be synthesized. Topographic maps using this technique have been demonstrated by Goldstein *et al.* [8], Gabriel *et al.* [9], and Gabriel and Goldstein [3].

The amount of decorrelation observed in these repeat-pass interferometers is important for two reasons. First, the amount of surface change over time describes processes occurring on time scales of the orbit repeat time and size scales on the order of a radar wavelength. Measurement of interferometer correlation thus provides a means to sense remotely a wide variety of surficial processes such as vegetation growth, glacier motion, permafrost freezing and thawing, and soil moisture induced effects.

The second area of interest in understanding temporal decorrelation is that it constitutes an important error source in the operation of a repeat pass geometry topographic mapping radar. The orbit selection will be driven by a combination of tolerable error levels, the attainable baseline, and the expected decorrelation with time of signals from the regions of interest to be mapped. Since this implementation approach may be employed using existing and planned general purpose radar satellites such as SEASAT, ERS-1, and RADARSAT, it is attractive in achieving the widest possible utilization of those systems.

We note here that there exists a class of radar interferometers specifically designed for measurement of radar echo phase differences on repeat images separated in time by less than a second, that is many times shorter than the temporal baselines we consider below. These are the "along-track" or "front–back" interferometers implemented on aircraft for the measurement of ocean surface motion such as currents or swell wave spectra (see Goldstein and Zebker [10] or Goldstein *et al.* [11] for a description of such instruments and their application). Since the geophysical phenomena for decorrelation of ocean surfaces are quite different than those for land processes, we defer a description of these to a later work, and will not consider them further.

II. Background

Coherent radar echoes, that is, those with measurable phase and amplitude, will be correlated with each other if each represents nearly the same interaction with a scatterer or set of scatterers. For imaging radars, another way of stating this is that the observed "speckle" patterns are similar. Speckle, according to a widely used model originally developed for laser scattering, may be modeled by postulating that at least several scattering centers are present in each resolution cell of the radar image; the total scattered field is then the coherent sum of the individual fields from each scattering center. If the scatterers are randomly positioned within the cell, and the cell is assumed to have dimension many wavelengths in size, the phase of each will be random and the sum will be well characterized by a zero mean, complex Gaussian random number with variance proportional to the average radar cross section of the surface.

Even though the radar signal in this case possesses Gaussian statistics, if we duplicate the radar imaging experiment at a later time but do not alter the position or cross section of the subresolution scatterers, the received signal will be identical to the original signal. In this sense, the signal is a spatially random process, but slowly varying with time, and repeated echoes will be highly correlated because variation is slow compared with the repeat observation frequency.

This does not imply that all observations of the same resolution cell will be correlated, however, as altering the observation geometry leads to decorrelation as the apparent relative positions of the scatterers change. Thus additional constraints on the repeat incidence and aspect angles are required for observation of echo correlation, but careful data acquisition and processing can minimize these effects. We will quantify the decorrelation due to each of these effects below.

In this paper we are concerned with the measurement of radar echo correlation and its interpretation in terms of the above effects. In particular, we would like to separate decorrelation due to actual changes of the target from that dependent on sensor geometry. In this manner we may infer geophysical properties of the surface without being confused by instrumental effects. In addition, understanding the sensor effects permits a more effective and useful system design and performance analysis, resulting in a controlled and quantified error budget.

For the purposes of this paper we will refer to the sensor geometry effects as spatial in nature and those due to target change as temporal effects, as the dominant source of decorrelation for a well-designed system observing a truly stationary target is spatial baseline noise caused by viewing the surface with two antennas at slightly different aspect angles. This is the effect which has been described by Li and Goldstein [4] and by Rodriguez and Martin [5]. The change in the target surface with time, the temporal effect, then causes additional decorrelation which is related only to properties of the surface.

III. Theory

We consider here the three sources of decorrelation introduced above: spatial baseline decorrelation, decorrelation due to rotation of the target between observations, and decorrelation from surface motion of the individual scattering centers within each resolution element. Two derivations of baseline decorrelation have been presented previously by Li and Goldstein [4] and by Rodriguez and Martin [5]; here for clarity we rederive the main results in a slightly different form and in addition obtain a Fourier transform relation between the correlation function and the system impulse response. We will verify the results by observation in the next section, and present data indicating the dependence of phase error on system parameters. For rotation, we find a similar transform relation and also present a numerical calculation of the decorrelation as a function of angle. We then verify that it is not important for the data analysis described in the next section. Finally, for the temporal decorrelation we plot decorrelation as a function of the degree of motion of the individual scatterers. In each case, we show the dependence of the correlation function on parameters of either the sensor or the target, as appropriate.

A. Overview

Consider two radar signals s_1 and s_2 acquired by two antennas observing the same target at the same time, but with different receivers. If we model the signals as consisting of a correlated part c common to the signal at both antennas and also of thermal noise parts n_1 and n_2, such as

$$s_1 = c + n_1$$

$$s_2 = c + n_2 \tag{1}$$

then we may evaluate the correlation $\rho_{thermal}$ between them as a function of noise in the usual manner:

$$\rho_{thermal} = \frac{\langle s_1 s_2^* \rangle}{\sqrt{\langle s_1 s_1^* \rangle \langle s_2 s_2^* \rangle}} \tag{2}$$

where $\langle \cdot \rangle$ denotes ensemble averaging. Since the noise and signal are uncorrelated, we obtain

$$\rho_{thermal} = \frac{|c|^2}{|c|^2 + |n|^2} \tag{3}$$

Noting that the thermal signal-to-noise ratio (SNR) is $\frac{|c|^2}{|n|^2}$, (3) may be equivalently written

$$\rho_{thermal} = \frac{1}{1 + SNR^{-1}} \tag{4}$$

Next, we generalize (1) by including a term representing that portion of the signal which is uncorrelated between antennas due to, say, spatial baseline decorrelation— a result of nonidentical viewing directions (see below). Then

$$s_1 = c + d_1 + n_1$$

$$s_2 = c + d_2 + n_2 \tag{5}$$

where c is the correlated part of the return, d_i is the uncorrelated part exclusive of thermal noise, and n_i again represents thermal noise. We now can calculate the correlation $\rho_{spatial}$ in the infinite SNR case:

$$\rho_{spatial} = \frac{|c|^2}{|c|^2 + |d|^2} \tag{6}$$

and also the correlation if thermal noise is included (these follow from simple application of (2) and (5) above):

$$\rho_{spatial+thermal} = \frac{|c|^2}{|c|^2 + |d|^2 + |n|^2} \tag{7}$$

Since the signal itself consists of both the correlated and decorrelated components, the SNR is $\frac{|c|^2+|d|^2}{|n|^2}$, thus (7) may be written

$$\begin{aligned}\rho_{spatial+thermal} &= \frac{|c|^2}{|c|^2 + |d|^2} \cdot \frac{|c|^2 + |d|^2}{|c|^2 + |d|^2 + |n|^2} \\ &= \frac{|c|^2}{|c|^2 + |d|^2} \cdot \frac{1}{1 + SNR^{-1}} \\ &= \rho_{spatial} \cdot \rho_{thermal}\end{aligned} \tag{8}$$

A similar argument leads to a further, and final, generalization for a pair of signals consisting of a correlated part, a decorrelated part due to spatial decorrelation, and a decorrelated part due to temporal phenomena, yielding the following for the total observed correlation:

$$\rho_{total} = \rho_{temporal} \cdot \rho_{spatial} \cdot \rho_{thermal} \tag{9}$$

We note that this derivation incorporates an assumption that the thermal noise powers at each antenna are equal, and that it is a trivial extension of the above to account for the situation for differing noise levels.

In summary, if any three of the quantities in (9) are known, the fourth may be determined. For data analyzed in this paper, we know quite well our imaging geometry and signal to noise ratio and can measure the total correlation ρ_{total}, therefore, the temporal component, which contains the information about the target, may be inferred. In the rest of this section we will present theoretical bases useful in determining the various correlation parameters.

B. Spatial Baseline Decorrelation

In order to determine the spatial decorrelation $\rho_{spatial}$, we need to calculate, from knowledge of our imaging geometry, what fraction of the received radar echo should be correlated between antennas. In this case, we know the interferometer baseline and need to determine the correlation as a function of that baseline.

We first derive a Fourier transform relation between the radar impulse response and the baseline decorrelation function

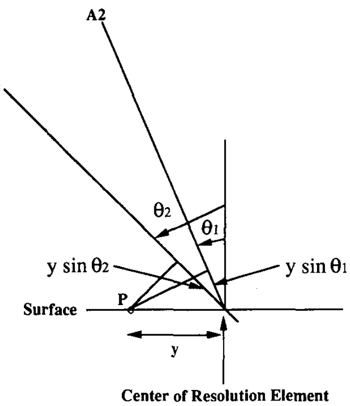

Fig. 1. Interferometer imaging geometry. Radar antennas A1 and A2 both illuminate the same patch of ground centered at $y = 0$. Incidence angles θ_1 and θ_2 result in phase offsets for all points P displaced by distance y of $y \sin\theta_1$ and $y \sin\theta_2$, respectively. Difference of these phases is measured interferometer phase.

as a function of the difference in viewing angles of the two interferometer antennas. Consider a radar interferometer operating with geometry as shown in Fig. 1 where two antennas A1 and A2 illuminate a patch on the surface at incidence angles θ_1 and θ_2, respectively. The along-track (azimuth) distance is x and the across-track (ground range) distance is y; the distance from the sensor itself to the center of a resolution element is r. Then the signal s_1, measured in the final processed image at position (x_0, y_0), from a radar antenna A1 may be represented as

$$s_1 = \int\int f(x - x_0, y - y_0) \exp\{-j\frac{4\pi}{\lambda}(r + y\sin\theta_1)\} \cdot W(x, y)dxdy + n_1 \tag{10}$$

where $f(x, y)$ represents the complex backscatter at each point on the surface, λ is the radar wavelength, $W(x, y)$ is the system impulse response, and n_1 is the noise associated with the receiver. Similarly, the signal from antenna A2 is

$$s_2 = \int\int f(x - x_0, y - y_0) \exp\{-j\frac{4\pi}{\lambda}(r + y\sin\theta_2)\} \cdot W(x, y)dxdy + n_2 \tag{11}$$

The cross-correlation of the two signals, from which we determine the interferometer phase, is thus

$$s_1 s_2^* = \int\int\int\int f(x - x_0, y - y_0) f^*(x' - x_0, y' - y_0) \exp\{-j\frac{4\pi}{\lambda}y(\sin\theta_1 - \sin\theta_2)\} W(x, y) W^*(x', y') dxdydx'dy' \tag{12}$$

If the interferometer is arranged such that the range r is unequal at the two antennas only the mean phase of the correlation changes, but not the correlation magnitude.

Now, if the surface is taken to consist of uniformly distributed and uncorrelated scattering centers, then

$$\langle f(x, y) f^*(x', y')\rangle = \sigma^0 \delta(x - x', y - y') \tag{13}$$

where σ^0 is the average radar cross section, (12) reduces to

$$\langle s_1 s_2^* \rangle = \sigma^0 \int\int \exp\{-j\frac{4\pi}{\lambda} y \cos\theta \; \delta\theta\} |W(x,y)|^2 dx dy \tag{14}$$

where θ is the average look angle and $\delta\theta = \theta_1 - \theta_2$. The exponential term, since it is linear in y, can be interpreted as a Fourier kernel and thus we have a transform relation between the correlation function and the radar system impulse response; the correlation function is simply the transform of the intensity impulse response.

For the typical radar model where the impulse response is approximately

$$W(x,y) = \mathrm{sinc}(x/R_x)\mathrm{sinc}(y/R_y) \tag{15}$$

where R_x and R_y are the azimuth and range resolutions, and the sinc function is taken as $\frac{\sin \pi x}{\pi x}$, evaluation of (14) followed by normalization leads to the spatial baseline decorrelation function

$$\rho_{spatial} = 1 - \frac{2\cos\theta \; |\delta\theta| R_y}{\lambda} \tag{16}$$

The correlation function, which from (14) is simply the Fourier transform of the impulse response intensity, falls off linearly as $\delta\theta$, the difference in look angle for the two antennas, increases. Equivalently, this effect can be described in terms of the antenna baseline separation B in meters (assumed to be in the horizontal direction only) by

$$\rho_{spatial} = 1 - \frac{2|B| R_y \cos^2\theta}{\lambda r} \tag{17}$$

The minimum value of B for which for which $\rho_{spatial}$ equals zero is the critical baseline B_c, and occurs when the change in look angle between the two passes is sufficient to cause backscatter from each pixel to become completely uncorrelated. Specifically,

$$B_c = \frac{\lambda r}{2 R_y \cos^2\theta} \tag{18}$$

In practice, the impulse response may also be modified by the nonideal characteristics of various elements in the radar itself as well as by windowing used during the processing, altering the baseline decorrelation function given in (17).

C. Decorrelation Due to Rotation

Another geometrical sensor effect that leads to decorrelation is rotation of the target with respect to the radar look direction. In other words, we cannot illuminate the same patch of surface from two different aspect angles and expect the signals to be fully correlated. To understand this source of decorrelation noise, consider a resolution element as shown in Fig. 2. Each scattering center at polar location (δ, ϕ) rotates to position $(\delta, \phi + d\phi)$. Transformation to rectangular coordinates $x = \delta\cos\phi$, $y = \delta\sin\phi$ permits us to express the change in position on the surface as a change in range; if the distance to a point before rotation is $r + \delta\sin\theta\sin\phi_1$, the distance after a small rotation $d\phi = \phi_1 - \phi_2$ is $r + \delta\sin\theta\sin\phi_2$. As the patch is rotated slightly, the range to and hence phase of each scattering center changes slightly, and their coherent sum will vary.

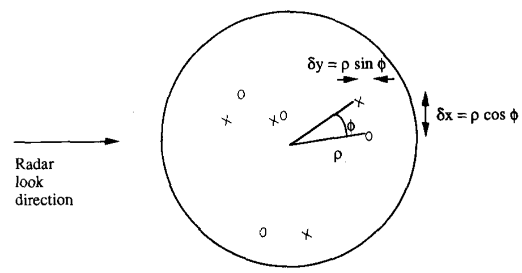

Fig. 2. Rotation of a resolution element by angle ϕ moves scattering centers from initial positions x to new positions o. Across-track component of displacement then yields slightly different phase shift for each scattering center, resulting in signal decorrelation.

We consider again two radar signals s_1 and s_2, representing the echo from a resolution element before and after rotation, respectively. By analogy with (12) above the cross-correlation of the two signals may be expressed as

$$s_1 s_2^* = \int\int\int\int f(x - x_0, y - y_0) f^*(x' - x_0, y' - y_0) \exp\{-j\frac{4\pi}{\lambda}\delta\sin\theta(\sin\phi_1 - \sin\phi_2)\} W(x,y) W^*(x',y') dx dy dx' dy' \tag{19}$$

and we obtain

$$\langle s_1 s_2^* \rangle = \sigma^0 \int\int \exp\{-j\frac{4\pi}{\lambda} x \sin\theta \; d\phi\} |W(x,y)|^2 dx dy \tag{20}$$

This second Fourier transform relation leads to the following expression for the rotation-induced decorrelation for $\frac{\sin x}{x}$ azimuth impulse response:

$$\rho_{rotation} = 1 - \frac{2\sin\theta |d\phi| R_x}{\lambda} \tag{21}$$

We have verified this result numerically by first determining a set of scattering centers randomly located within a resolution cell, and then altering the position of each according to a rotation of the entire cell. This process is repeated many times (1000) to obtain the ensemble average, which we present in Fig. 3. The relevant parameters here correspond to data acquired by the SEASAT satellite operating at L-band (λ = 24 cm, for a system description see observation section below), and also for a C-band (λ =5.66 cm) system in a similar orbit. Thus the C-band results will be approximately correct in assessing the performance of the ERS-1 radar satellite in interferometric applications.

The simulation results indicate that the signal decorrelates with angle, and nearly completely after rotation of about 2.8° at L-band and after about 0.7° at C-band, in agreement with (21). The functional dependence of the correlation depicted in Fig. 3 is not quite linear as we used a truncated impulse response for computational reasons, thus the transform of the azimuth response is not a triangle function. We have, however, preserved an "equivalent-width" response so that the critical rotation angle remains about the same.

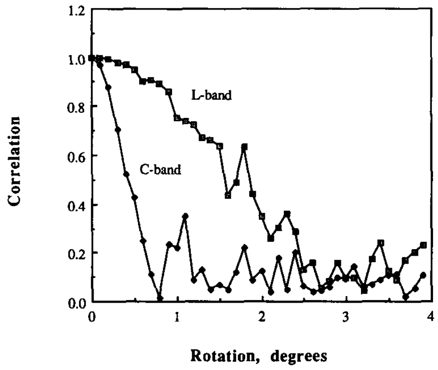

Fig. 3. Simulation results indicating dependence of correlation on rotation of resolution elements. Assumed L-band system parameters are those for SEASAT , while C-band parameters are similar but for wavelength of ERS-1 radar. Complete decorrelation results after a rotation of 2.8° at L-band, 0.7° at C-band.

In fact, the SEASAT data we analyze in this paper were acquired with orbits that are parallel within 0.02° and thus the decorrelation we observe from this effect is minimal.

D. Temporal Decorrelation

The final decorrelation source of interest here is the temporal effect, which follows from physical changes in the surface over the time period between observations. For the SEASAT case, the orbit repeat time was 3 days, so that temporal baselines of 3 days, 6 days, 9 days, and so forth are available. Since calculation of this effect depends on detailed changes of a given surface type, we present here only a sample calculation assuming Gaussian-statistic motion as a guide and leave predictive application-specific theories for later work. In the observation section of the paper which follows we will experimentally characterize temporal decorrelation from unvegetated, lightly vegetated, and heavily forested surfaces.

Once again, we begin with the expression for the correlation between two signals s_1 and s_2 (see (22) below) where we have generalized the backscatter function $f(z, y, z)$ to account for three-dimensional variability (volume scatter, important for vegetation models), and included terms related to change horizontal position δy and change in height δz of a scatterer in the exponential kernel. If we assume that changes in position of a scatterer are unrelated to the initial position, and are characterized by independent probability distributions $p_y(\delta y)$ and $p_z(\delta z)$, (22) reduces to (23) below.If the probability distributions are Gaussian, then after normalization the integral yields

$$\rho_{temporal} = \exp\{-\frac{1}{2}(\frac{4\pi}{\lambda})^2(\sigma_y^2 \sin^2\theta + \sigma_z^2 \cos^2\theta)\} \quad (24)$$

For the SEASAT geometry where the nominal incidence angle is 23°, the contribution from displacements in z is greater than that for displacements in y as indicated by the geometrical factors in (24). In other words, we expect greater sensitivity to vertical changes than to horizontal changes for incidence angles less than 45°, and thus surfaces with significant volume scattering, such as forests, should decorrelate most rapidly with time.

We again verify this result by simulation, where we restrict motion to the surface plane (δy only) for simplicity. For our sample calculation we alter the location of the scattering centers within a volume in a random direction by adding to each location a complex Gaussian distance of specified rms motion, thus the direction of each motion is uniformly random in angle. In Fig. 4 we plot temporal decorrelation at two wavelengths as a function of rms motion and also indicate the analytical result, where the wavelengths used are 0.24 m (L-band) and 0.0566 m (C-band). The remaining radar parameters are typical for SEASAT. We note that in this case 10 cm of rms motion is needed for complete decorrelation at L-band while only 2–3 cm rms motion decorrelates C-band signals.

We have here considered only random motions, that is, each scattering center moves independently of all others. If in fact the scatterers move together in one preferred direction, then instead of decorrelation a systematic phase shift would occur. This idea has been proposed and applied to measurement small surface changes (see, for example, [9]).

E. Implications for Topographic Mapping

Our final theoretical result is to assess the effect of decorrelation on the accuracy of inferred topographic maps. The major implication of decorrelation in an interferometer is that it adds noise to the radar echoes, increasing the standard deviation of inferred phase estimates and hence the derived height values. This topic has been previously addressed by Zebker and Goldstein [2], Li and Goldstein [4], and Rodriguez and Martin [5], although they did not consider the additional noise due to temporal decorrelation. Using the approximate formula given by Rodriguez and Martin [5, eq. 31], we can relate the phase standard deviations to height errors as follows:

$$\sigma_h = \frac{\lambda\rho\tan\theta}{4\pi B}\sigma_\phi \quad (25)$$

$$s_1 s_2^* = \int\int\int\int\int\int f(x - x_0, y - y_0, z - z_0) f^*(x' - x_0, y' - y_0, z' - z_0)$$
$$\exp\{-j\frac{4\pi}{\lambda}(\delta y \sin\theta + \delta z \cos\theta)\} W(x, y) W^*(x', y') dx dy dz dx' dy' dz' \quad (22)$$

$$\langle s_1 s_2^* \rangle = \sigma^0 \int\int \exp\{-j\frac{4\pi}{\lambda}(\delta y \sin\theta + \delta z \cos\theta)\} p_y(\delta y) p_z(\delta z) d\delta y d\delta z \quad (23)$$

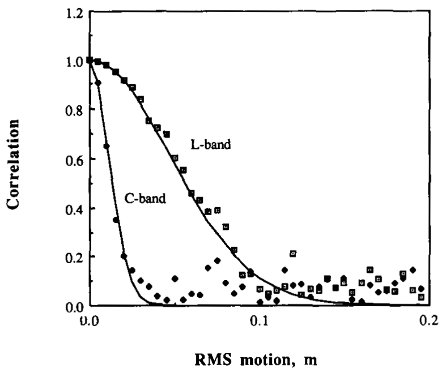

Fig. 4. Simulation results indicating dependence of correlation on random motion of scattering centers within resolution elements (points), with theoretical predictions (solid lines). As in previous figure, assumed L-band system parameters are those for SEASAT, while C-band parameters are those for wavelength of ERS-1 radar. Complete decorrelation results after rms motion of 10 cm at L-band, 2–3 cm at C-band.

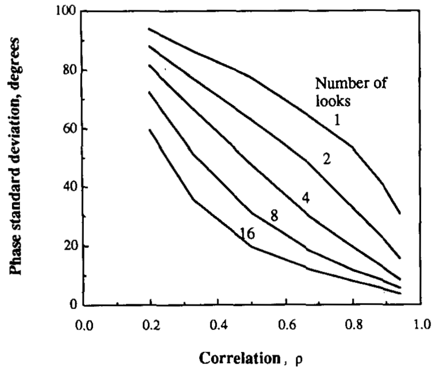

Fig. 5. Sensitivity of phase standard deviation to correlation and number of looks in processor. Increasing number of looks is an effective means to reduce statistical variation, especially for the first eight looks or so.

where ρ is range, θ is the look angle, B is the interferometer baseline, λ is the radar wavelength, and σ_h and σ_ϕ are the standard deviations of height and phase, respectively.

We have calculated, and present in Fig. 5, the expected phase standard deviations as a function of the interferometric radar system parameters of correlation and number of looks, where by number of looks we refer to the number of resolution elements averaged spatially in the complex interferogram to reduce statistical variations. For example, if the correlation ρ_{total} is 0.8 and we average four resolution elements in the interferogram, the resulting phases are determined with an uncertainty of 21°. Equation (25) may then be used to infer the resulting height precision, which would be 5 m for SEASAT operating with a baseline of 500 m. Note that "taking looks" is a particularly effective means to reduce errors when the number of looks is less than eight or so; therefore, systems should be designed with this in mind.

F. Observations

In this section, we present observations of decorrelation using SEASAT data, and derive a topographic map of a region in Oregon containing both lightly vegetated and heavily forested areas. First, we will describe the relevant parameters of the radar system and satellite orbit geometry. Next, we show measured spatial baseline decorrelation from data acquired over Death Valley, and temporal decorrelation from that site and several areas in the Oregon image. Finally, we derive the topographic map and estimate its accuracy over the several surface types included in the image.

TABLE I
SEASAT ORBIT PARAMETERS

Orbit Number	Date	Long. Asc. Node	Inclination
1226	Sept. 20	255.9989	108.0202
1269	Sept. 23	255.9930	108.0076
1312	Sept. 26	255.9885	108.0176
1355	Sept. 29	255.9863	108.0294
1398	Oct. 2	255.9868	108.0196
1441	Oct. 5	255.9896	108.0071
1484	Oct. 8	255.9950	108.0166

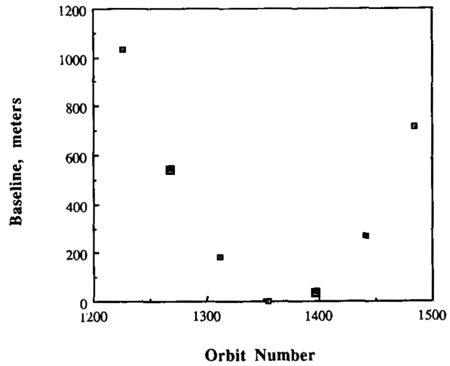

Fig. 6. Relative offsets of SEASAT orbits. Interferometer baseline for any pair of orbits may be found by difference of offsets for that pair. These values approximately correct for western U.S.

1) SEASAT Parameters: The data shown here were acquired by the SEASAT synthetic aperture radar satellite over a period from September 20–October 8, 1978. The corresponding orbit numbers range from 1226 to 1484. The SEASAT orbit altitude of 800 km provided for a nearly exact repeat track every 43 orbits (3 days). Orbital data are given in Table I.

A plot of approximate orbit offsets in meters over the western U.S. is shown in Fig. 6, where the independent variable is orbit number and the dependent variable is the relative offset of each orbit to orbit 1355 (chosen arbitrarily). Thus to find the interferometer baseline for any given pair of orbits, the relative locations from Fig. 6 must be differenced. The orbit position varies approximately quadratically with time. This should be kept in mind during the analyses presented below, when we are isolating observed temporal effects from spatial effects—the available time and space baselines are uncorrelated with each other.

The SEASAT radar consisted of a nominal 1-kW transmitter, operating at 1275 MHz and transmitting 33 μs pulses at a rate of 1647 pulses per second. The transmit waveform was range coded by a linear FM signal for 19-MHz bandwidth. Data were transmitted to Earth using an analog downlink, and offset video signals were digitized on the ground to 5-bit accuracy at a sample rate of about 45.5 MHz. These samples were then processed on a general purpose computer using a conventional range/Doppler algorithm. Complex, single look high resolution pixels were generated, with a typical scene size of 1024 pixels in range by 4096 pixels in azimuth and corresponding to approximately 16 km by 16 km on the ground. As stated above, the nominal radar incidence angle was 23°.

2) Baseline Decorrelation: The arid, unvegetated floor of Death Valley in California serves as an ideal target for measurements of baseline decorrelation. The relatively strong backscatter from rough portions of the valley floor results in a high SNR and therefore minimizes the effect of the $\rho_{thermal}$ term in (9). More importantly, changes in the surface on a time scale of days or weeks are negligible, minimizing $\rho_{temporal}$ as a possible source of decorrelation. As a result, the observed correlation ρ_{total} is in effect a direct measure of $\rho_{spatial}$ and should fall off nearly linearly as the baseline B is increased. Interferograms obtained using small baselines are relatively free from degradations caused by baseline decorrelation, but are characterized by broad fringes and reduced accuracy in the resulting height maps. The lengths of the 21 baselines which can be synthesized using the seven SEASAT orbits given in Table I range from approximately 50 to 1100 m.

We estimated the critical baseline for our SEASAT data at about 4500 m by first estimating the system impulse response and then computing its Fourier transform as indicated above. Since our scenes of Death Valley, CA and Bend, OR did not contain any known point reflectors, we used the impulse response determined by the JPL SEASAT project which was documented in a JPL internal report [12]. They found that data from a calibration site at Goldstone Dry Lake in California were well modeled by an unweighted $\sin(x)/x$ function with intensity half-power width of 25 m. The transform of this response, as discussed above, is a linearly decreasing function which equals zero for a baseline of approximately 4500 m.

In order to compare observed baseline decorrelation with this theoretical estimate, we first formed six interferograms using images of Cottonball Basin in Death Valley acquired during orbits 1226, 1355, 1441, and 1484. For each pair of images we used a statistical correlation technique to estimate the relative offset and then resampled the data to coregister the images. Next, we selected regions of Cottonball Basin characterized by flat or smoothly sloping topography and therefore by straight, evenly spaced fringes in the interferograms. Using an iterative procedure, we identified and then removed from one of the images the phase ramp best corresponding to the observed fringes. Finally, for each region we calculated the correlation ρ_{total} $(= \rho_{spatial})$ between the images using the pixels within the area of interest. The resulting correlations, plotted in Fig. 7, show the near linear dependence on baseline expressed in (17). A critical baseline value of $B_c = 3200$ m, obtained by fitting a linear function to these data, is in very rough agreement with the value of 4500 m calculated using (17).

Note from Fig. 7 that our observed values of correlation fall below the theoretical expectation, which leads to a low estimate of the critical baseline. What this implies is that there

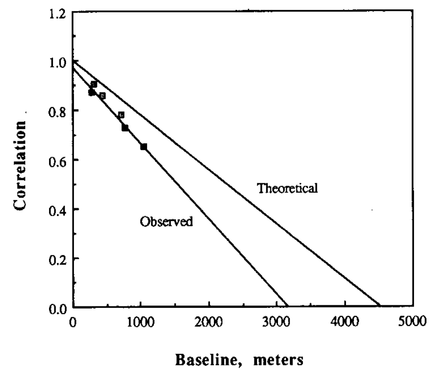

Fig. 7. Theoretical and empirically determined spatial baseline decorrelation functions. Ideal impulse–response analysis indicates a critical baseline, that is the baseline for which correlation equals zero, of 4500 m, while data fits to a value of 3200 m. The discrepancy is due to unmodeled decorrelation sources in the radar system. We thus use the empirically derived model for later analysis in order to compensate for these unkown error sources.

are additional unmodeled sources of decorrelation in our data. These sources can be, for example, interpolation noise in the processor or analysis routines, or that the impulse response we assumed is narrower than the true impulse response. Therefore, in the remainder of this paper we will model the baseline decorrelation by the empirically-derived function with a critical baseline of 3200 m rather than the theoretically ideal model. This approach allows us to isolate the temporal phenomena from any unknown processor-induced effects.

3) Temporal Decorrelation: We next considered an area in central Oregon characterized by diverse topography and containing both heavily forested areas and partially vegetated and bare lava flows. In contrast with Death Valley, we would expect more physical changes in the surface itself over the 18 days spanned by the seven SEASAT orbits. Another difference involved the topography and therefore the size of the areas over which we could consider decorrelation. The technique of removing fringes by applying a phase ramp to one of the images works only when the surface topography can be approximated by a plane. Many regions of Death Valley are indeed quite flat and are therefore well-suited to this approach. For data collected over the Oregon site, however, the selected areas must be large enough to produce statistically reliable results, but small enough so that the terrain can be approximated as flat. An alternative but less practical approach could involve utilizing arbitrarily large areas over which the fringes are removed using detailed knowledge of the true topography. Even if sufficiently detailed digital elevation maps were available, the increase in computational complexity would probably not justify the improvement in the results. We found it difficult to obtain good correlations using areas larger than about 20 × 20 pixels (a pixel corresponds to about 17 m) and used areas measuring 10 pixels on a side for most of this work.

Using a procedure identical to that described in the previous section, we processed data for six SEASAT passes (central Oregon was not imaged during orbit 1355) and formed 15 interferograms. We then selected both forested and unvege-

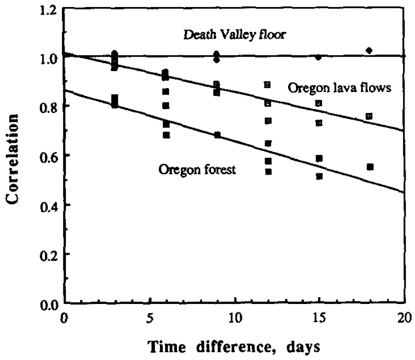

Fig. 8. Temporal decorrelation as a function of time for three surfaces. The floor of Death Valley exhibits no significant decorrelation over our 18-day observation period. The lightly vegetated and unvegetated lavas in Oregon show some temporal effects, and the heavily forested regions show the most temporal decorrelation. Even after 18 days, however, the correlation associated with the forested areas is still 0.5, enough for reasonably reliable topographic maps to be generated.

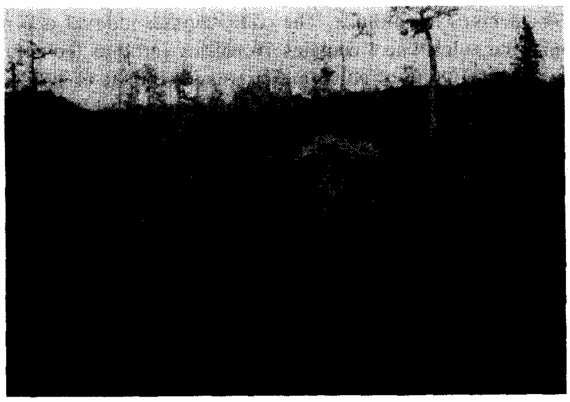

Fig. 9. Photograph of lava areas from which correlation values were measured. Note that the surface is rather devoid of vegetation, thus we do not understand the physical mechanism for the observed, albeit minor, decorrelation with time.

tated lava areas for analysis. After determining and removing from each interferogram the appropriate phase ramp for each small area, we calculated ρ_{total} and removed the contributions due to $\rho_{thermal}$ and $\rho_{spatial}$. The value which remained was $\rho_{temporal}$, which we interpret as an indication of the degree to which the area had changed in the time between the two images. A value of $\rho_{temporal} = 1$ indicates no change, while surface changes alter the exact complex backscatter and cause decorrelation, reducing $\rho_{temporal}$. By plotting $\rho_{temporal}$ as a function of time difference between images, an indication of the presence and degree of surface change results.

We present our temporal decorrelation results in Fig. 8. To verify that we had succesfully eliminated system errors which could give erroneous results suggesting gradual surface change where none existed, we first examined an area in Death Valley. Given the absence of precipitation and other factors which could change the nature of the surface on a time scale of several weeks, we expected to find no significant temporal decorrelation. As the plot of Fig. 8 shows, the surface of Death Valley remains fully correlated over our 18 days of observations, indicating minimal residual influence of system errors and demonstrating that the surface does remain unchanged. We next implemented a similar analysis on data acquired over forests and lava flows at the Oregon site. The forest decorrelates in what appears to be a linear fashion, reaching $\rho_{temporal} \approx 0.5$ for a time difference of 18 days. This is plausible given the volume scattering occuring for vegetated targets (see [13], or [14], for example, radar scattering models incorporating volume scattering from canopies), in which wavelength-order changes in the positions of branches significantly alter the speckle and therefore the correlation.

The temporal decorrelation results for the lava data, also shown in Fig. 8, are more difficult to explain. The lava appears to decorrelate at approximately the same rate as the forest, but with a higher initial value. Although the results plotted in Fig. 8 represent only one forested area and one lava area, correlations calculated in other areas produce similar results — signals from both the forest and the lava appear to decorrelate at about the same rate, but with the lava echoes consistently exhibiting higher correlation than the forest.

We first suspected that the decorrelation of the lava might be due to a system error. However, the same SEASAT orbits were used to acquire data over both Death Valley and Oregon (overflight times for the two sites are separated by only 3 min), and the intereferograms of Death Valley show no sign of temporal decorrelation. Many other possible error sources, such as those involving estimation of the baseline or SNR, are unrelated to the time difference between pairs of images and would not produce the results of Fig. 8. We also considered the possibility that the lava surface was vegetated and that we were in fact seeing changes in this vegatation rather than in the lava itself. The lava flows in question are approximately 5000 years old, and in certain areas pockets of soil have collected, permitting growth of brush and some trees. A visit to the area, however, showed that much of the lava has remained completely bare, as shown in the photograph of Fig. 9. Weather is also unlikely to provide an explanation. Throughout the entire period spanning these orbits (late September to early October 1978) the weather was dry with temperatures reaching 25–30 °C during the day and dropping to 10–15° at night. In addition, the data were acquired at approximately the same local time for each pass (about 10:30 AM) rendering dew and thermal expansion unlikely sources of decorrelation. We are left with the possibilities that 1) there is some progressive error source unique to the Oregon images which we have not eliminated, or 2) that there is true change occurring in the lava. It is true that the Oregon lava is blockier than the smooth floor of Death Valley, but why that would effect the observed decorrelation is unclear.

4) Topographic Map: In Fig. 10 we present a conventional radar image and also the interferometrically-produced topographic map of the study area in Oregon derived from a single pair of SEASAT passes (orbits 1226 and 1269). This pair was chosen to maximize spatial baseline (484 m) and minimize temporal baseline (3 days). In the figure, the brightness of each point is related to the magnitude of radar backscatter while the color denotes the altitude. The color contour interval is 6 m, while the color wheel contains 16 entries and thus the colors repeat every 96 m of altitude. The image consists of 1024 by 1024 points each with ground spatial dimensions 17 by 17 m, thus the image is slightly greater than 17 km on a side.

We note that relatively noise-free topography is available everywhere in the image, even over the most heavily forested area. These data were averaged to 16 looks. Given the 484-m baseline we estimate $\rho_{spatial}$ from (17) at approximately 0.85, and since the time separation was 3 days, from Fig. 8 we would expect approximately to observe $\rho_{temporal}$ of 0.97 and 0.8 over the lightly vegetated lavas and heavily forested areas, respectively. Thermal contributions are negligible for this scene. The total correlations ρ_{total} for the two types of targets are then 0.82 and 0.68. Examination of Fig. 5 yields phase standard deviations of 7 and 12°, respectively, for the lightly vegetated and heavily forested areas. Finally, using (25) we estimate the statistical variation contribution to the error in height to be 1.5 m over the lightly vegetated lava regions and 2.6 m over the forest. Of course, the actual accuracy is several times worse than this as the error budget is dominated by systematic errors such as uncertainty in baseline knowledge. Our main conclusion here is that if the temporal baseline is constrained at a few days or less, the additional height error due to temporal changes on the surface are not significant contributors to the overall error.

Of course additional optimization may be applied to the data of Fig. 10. For example, if additional height acuity is needed, we could average spatially to obtain more "looks," if maximum spatial resolution is not required.

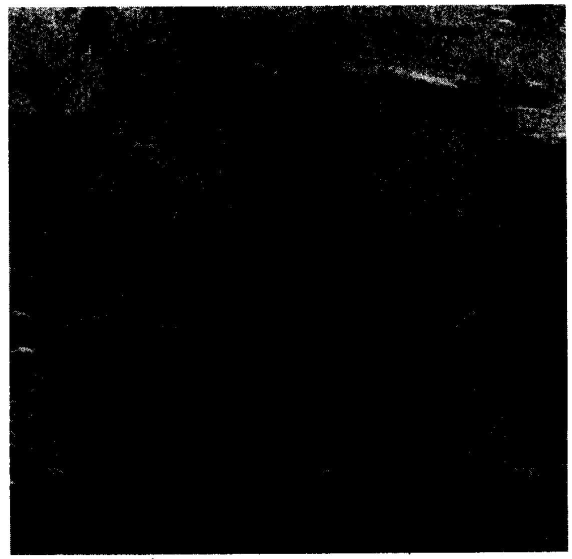

(a)

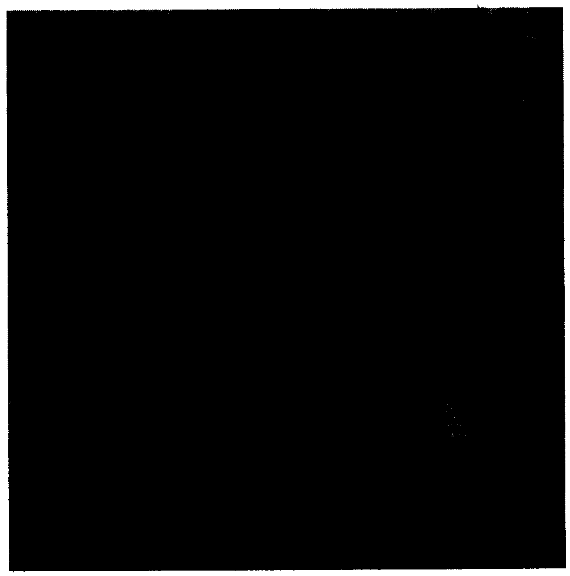

(b)

Fig. 10. Radar image (a) and interferometrically derived topographic map (b) of Oregon forested area. Height contour levels are 6 m/color, or 96 m for one complete color cycle. The topography is clearly visible even in the most heavily forested regions. The layed over cones in the radar image are seen to be rectified in the topographic map, demonstrating that with three-dimensional data cartographically correct maps may be generated. The irregular border at the bottom of the topographic map is a result of the nonlinear stretch applied to rectify the image.

IV. Summary

Correlation in pass-to-pass, interferometric radar can be degraded by thermal noise, lack of parallelism between the radar flight tracks, spatial baseline noise, and surficial change. The effects of decorrelation due to thermal noise can be easily evaluated and removed, while those due slight angular changes between flight tracks are negligible for data acquired using near-repeat orbits. Spatial baseline and rotation-induced decorrelation can be derived using the Fourier transform of the impulse response intensity, and increase linearly with baseline or rotation in an ideal system. Empirical results obtained using images of Death Valley confirm that, as the baseline increases, the overall correlation decreases due to spatial baseline noise. As the effects of these three sources of decorrelation can be quantified, their contributions to the observed overall correlation can removed, yielding a measure of the temporal decorrelation due to change in the target itself. We have shown that areas of Cottonball Basin in Death Valley remained unchanged over the 3-week period for which we have data, while a heavily forested area in Oregon exhibited significant temporal decorrelation. Lava surfaces in central Oregon also appeared to decorrelate, although the reasons for this are uncertain. We generated a topographic map from the images of central Oregon and achieve statistical contributions to height accuracy of 1.5 m over unvegetated areas and 2.6 m over forest. Our results demonstrate that generation of height maps of heavily vegetated areas using pass-to-pass interferometry is practical provided that the time between passes is at most several weeks.

Acknowledgment

We would like to thank Soren Madsen and Dick Goldstein for many helpful suggestions and discussions about interferometer data analysis. We would also like to thank Soren for a careful reading of the manuscript.

REFERENCES

[1] L. C. Graham, "Synthetic interferometer radar for topographic mapping," *Proc. IEEE*, vol. 62, pp. 763–768, 1974.

[2] H. Zebker and R. Goldstein, "Topographic mapping from interfermetric SAR observations," *J. Geophys. Res.*, vol. 91, no. B5, pp. 4993–4999, 1986.

[3] A. K. Gabriel and R. M. Goldstein, "Crossed orbit interferometry: Theory and experimental results from SIR-B," *Int. J. Remote Sensing*, vol. 9., no. 8, pp. 857–872, 1988.

[4] F. Li and R. M. Goldstein, "Studies of multi-baseline spaceborne interferometric synthetic aperture radars," *IEEE Trans. Geosci. Remote Sensing*, vol. 28, pp. 88–97, Jan. 1990.

[5] E. Rodriguez and J. Martin, "Theory and design of interferometric SAR's," submitted to *Proceeding of the IEE*, 1991.

[6] H. A. Zebker, S. Vetrella, J. Martin, *et al.*, TOPSAR: The NASA/ASI airborne topographic radar mapper, in preparation.

[7] A. Moccia and S. Vetrella, "A tethered interferometric SAR for a topographic mission," in press, *IEEE Trans. Geosci. Remote Sensing*, 1991.

[8] R. M. Goldstein, H. A. Zebker, and C. Werner, "Satellite radar interferometry: two-dimensional phase unwrapping," *Radio Sci.*, vol. 23, no. 4, pp 713–720, July-Aug. 1988.

[9] A. K. Gabriel, R. M. Goldstein, and H. A. Zebker, "Mapping small elevation changes over large areas: differential radar interferometry," *J. Geophys. Res.* vol. 94, no. B7, 9183–9191, July 10, 1989.

[10] R. M. Goldstein and H. A. Zebker, "Interferometric radar map of ocean surface currents," *Nature*, vol. 328, no. 6132, pp. 707–709, Aug. 20, 1987.

[11] R. M. Goldstein, T. P. Barnett, and H. A. Zebker, "Remote sensing of ocean currents," *Science*, vol. 246, pp. 1282–1285, Dec. 8, 1989.

[12] S. H. Pravdo, B. Huneycutt, B. Holt, and D. Held, *SEASAT Synthetic Aperture Radar Data User's Manual*, JPL Publication 82–90, Jet Propulsion Laboratory, Pasadena, CA, Mar. 1, 1983.

[13] J. A. Richards, G. Sun, and D. Simonett, "*L*-band radar backscatter modeling of forest stands," *IEEE Trans. Geosci. Remote Sensing*, vol. GE-25, pp. 487–498, 1987.

[14] S. L. Durden, H. A. Zebker, and J. J. van Zyl, "Modeling and observation of forest radar polarization signatures," *IEEE Trans. Geosci. Remote Sensing*, vol. 27, pp. 290–301, Mar. 1989.

Howard A. Zebker (M'87–SM'89), for a photograph and biography, please see page 940 of this issue of the TRANSACTIONS.

John Villasenor (S'83–S'88–M'89), photograph and biography not available at the time of publication of this issue.